EUROPEAN ORGANISATION FOR NUCLEAR RESEARCH (CERN)

Submitted to: Eur. Phys. J. C

CERN-EP-2019-165
August 20, 2019

Measurement of ϕ meson production in $p + p$ interactions at 40, 80 and 158 GeV/c with the NA61/SHINE spectrometer at the CERN SPS

The NA61/SHINE Collaboration

Results on ϕ meson production in inelastic $p + p$ collisions at CERN SPS energies are presented. They are derived from data collected by the NA61/SHINE fixed target experiment, by means of invariant mass spectra fits in the $\phi \to K^+K^-$ decay channel. They include the first ever measured double differential spectra of ϕ mesons as a function of rapidity y and transverse momentum p_T for proton beam momenta of 80 GeV/c and 158 GeV/c, as well as single differential spectra of y or p_T for beam momentum of 40 GeV/c. The corresponding total ϕ yields per inelastic $p + p$ event are obtained. These results are compared with existing data on ϕ meson production in $p + p$ collisions. The comparison shows consistency but superior accuracy of the present measurements. The emission of ϕ mesons in $p + p$ reactions is confronted with that occurring in Pb + Pb collisions, and the experimental results are compared with model predictions. It appears that none of the considered models can properly describe all the experimental observables.

1 Introduction

The motivation for studying particle production in proton-proton collisions is twofold. Firstly, such data are necessary to characterize soft hadronic interactions and to develop phenomenological models which are then used to describe the observable final states. Particle yields (only) are generally well described by statistical particle production models, see e.g. Ref. [1], while complete particle spectra are computed in e.g. microscopic (string) models [2–4]. Secondly, they are considered as a trivial reference in the search for collective effects in heavy ion collisions at moderate energies. In this context the ϕ meson is one of the most interesting hadrons, because it consists of an s and an $\bar{s}$ valence quark with only small admixtures of light valence quarks. Its net strangeness vanishes, which means that in a pure hadron scenario, ϕ production is insensitive to strangeness-related effects. On the other hand, if partonic degrees of freedom are significant, the ϕ will behave like a doubly-strange particle. Therefore ϕ mesons are expected to play a key role in studies of phenomena related to the phase transition separating the confined hadron and deconfined parton phase, the quark-gluon plasma. The transition is considered to occur in heavy ion collisions in the lower CERN SPS energy regime [5]. Such parton matter may (can) be detected in the final state of nuclear collisions by studying the onset of medium effects which cannot be explained by hadron processes. Doubly-strange hadrons are considered to be sensitive to those medium effects. Thus the results on ϕ production at beam momenta of 40 GeV/c, 80 GeV/c, and 158 GeV/c presented in this paper serve as a pure hadron scenario reference for the comparison with results measured in nuclear collisions at the same energy.

Production of ϕ mesons has been measured in colliding systems ranging from $e^- + e^+$ to Pb + Pb reactions, and at energies from GSI SIS to CERN LHC accelerators. In this paper double differential yields of ϕ mesons produced in proton-proton collisions at 80 GeV/c and 158 GeV/c as well as single differential yields at 40 GeV/c are presented and compared with published experimental data on $p + p$ interactions [6–17], and on Pb + Pb collisions at the same energy [18]. For $p + p$ collisions, measurements exist of differential and total inclusive cross-sections at CERN SPS and ISR energies [6–9]. The NA49 collaboration published single differential spectra of rapidity and transverse momentum at the incoming beam energy of 158 GeV [10], allowing for direct comparison with the present work. At higher collision energies mainly the midrapidity region of ϕ production is known experimentally [12–16], with the exception of double differential cross-sections measured in the forward region by the LHCb experiment [17].

For the purpose of the comparison between $p + p$ and Pb + Pb reactions, the present analysis operates on multiplicities of ϕ mesons produced per inelastic $p + p$ collision rather than cross-sections. Note that the latter can be transformed into the former using tables of total (σ_{tot}) and elastic (σ_{el}) proton-proton cross-sections as a function of collision energy [19]:

$$n = \frac{\sigma}{\sigma_{\text{tot}} - \sigma_{\text{el}}}, \tag{1}$$

where n is the multiplicity per inelastic interaction while σ is the cross-section for ϕ production.

This paper is the fourth in a series of the NA61/SHINE collaboration presenting experimental results on particle production in $p + p$ interactions at CERN SPS energies. The relevant details of beam, target, experimental setup, and event selection were already described in previous publications [20–22]. Therefore Section 2 contains only a short description of the NA61/SHINE spectrometer, of the data samples, and of the event selection. Section 3 summarizes the data analysis and systematic errors. Section 4 presents and discusses the results of the present analysis together with the world data on ϕ production in $p + p$ and Pb + Pb collisions and compares them with calculations of the three microscopic models Pythia, Epos,

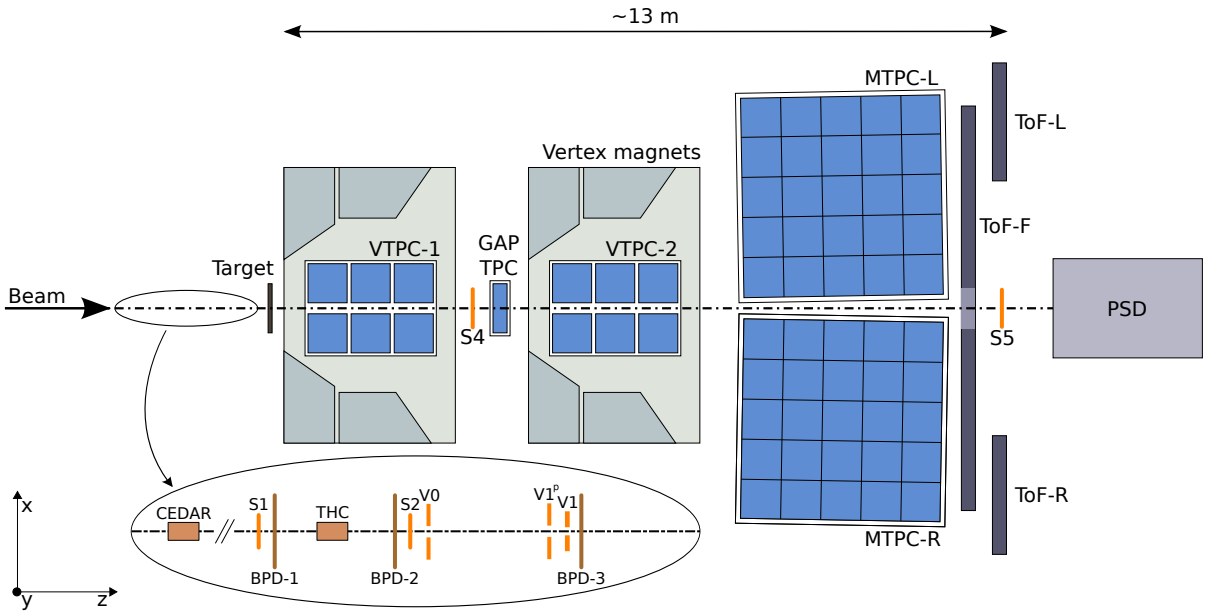

Figure 1: Schematic layout of the NA61/SHINE detector system (horizontal cut in the beam plane, not to scale). Also outlined are the coordinate system used in the experiment and the beam detector configuration used with secondary proton beams in 2009.

and UrQMD [2, 23–26]. The latter two are also designed to describe nuclear collisions. A summary in Section 5 closes the paper.

The following variables and definitions are used in this paper. The particle rapidity y is calculated in the collision center of mass system (cms), $y = 0.5 \ln[(E + cp_{\mathrm{L}})/(E - cp_{\mathrm{L}})]$, where E and p_{L} are the particle energy and longitudinal momentum, respectively. The transverse component of the momentum is denoted as p_{T} and the transverse mass m_{T} is defined as $m_{\mathrm{T}} = \sqrt{m^2 + (p_{\mathrm{T}}/c)^2}$ where m is the particle mass. The total momentum in the laboratory frame is denoted p and the collision energy per nucleon pair in the center of mass by $\sqrt{s_{NN}}$.

2 The NA61/SHINE experiment

NA61/SHINE is a fixed target experiment conducted in the North Area of the CERN Super Proton Synchrotron (SPS) accelerator complex. The detector system of NA61/SHINE, depicted in Fig. 1, is described in detail in Ref. [20]. The data studied in the present analysis were collected with secondary beams of positively charged hadrons at 40, 80 and 158 GeV/c. The latter were produced by 400 GeV/c protons extracted from the SPS onto a beryllium target in the slow extraction mode with a flat-top of 10 seconds. The secondary beam momentum and intensity was adjusted by proper setting of the H2 beam-line magnet currents and collimators. The beam was transported along the H2 beam-line towards the experiment. The precision of the bending power of the beam magnets was approximately 0.5%. The protons in the secondary hadron beam (58% at 158 GeV/c, 28% at 75 GeV/c and 14% at 40 GeV/c) were identified by two Cherenkov counters, a CEDAR (either CEDAR-W or CEDAR-N) and a threshold counter (THC). The CEDAR counter, using a coincidence of six out of the eight photo-multipliers placed radially along the Cherenkov ring, provided positive identification of protons, while the THC, operated at pressure lower than the proton threshold, was used in anti-coincidence in the trigger logic. Due to their

Table 1: Number of events recorded in 2009 and selected for the ϕ analysis.

p_{beam} [GeV/c]	recorded	selected
158	$3.5{\cdot}10^6$	$1.3{\cdot}10^6$
80	$4.5{\cdot}10^6$	$1.3{\cdot}10^6$
40	$5.2{\cdot}10^6$	$1.6{\cdot}10^6$

limited range of operation two different CEDAR counters were employed, namely for beams at 20, 31, and 40 GeV/c the CEDAR-W counter and for beams at 80 and 158 GeV/c the CEDAR-N counter. The threshold counter was used for all beam energies. This scheme allowed to select beam protons with a purity of about 99%. Beam particle trajectories were measured by a set of three beam position detectors (BPDs) used to determine the transverse position of the collision point. The beam trigger used the information from plastic scintillator and Cherenkov counters. The interaction trigger consisted of the beam trigger and a veto-signal from a 2 cm diameter scintillator (S4) placed approximately 4 m downstream from the target on the trajectory of the beam. This minimum bias trigger required that a valid beam proton is absent downstream of the target. There was, however, a non-negligible probability that a charged particle from an inelastic collision hits S4 and inhibits the recording of the associated event. This bias is taken into account by a Monte Carlo correction. The target was a liquid hydrogen vessel. It was a 20.29 cm long (2.8 % of nuclear interaction length) cylinder with a diameter of 3 cm. The liquid hydrogen had a density of approximately 0.07 g/cm^3.

The main components of the detection system used in the analysis are four large volume Time Projection Chambers (TPC). Two of them, called Vertex TPCs (VTPC), are located approximately 80 cm downstream of the target centered inside superconducting magnets which provide a maximum combined bending power of 9 Tm. Two further TPCs (MTPC) are placed side by side in the field free region behind the magnets. The TPCs are filled with Ar:CO_2 gas mixtures in proportions 90:10 for the VTPCs and 95:5 for the Main TPCs. Two walls of pixel Time-of-Flight (ToF-L/R) detectors are placed symmetrically to the beamline downstream of the Main TPCs. Each wall contains 891 individual scintillation detectors with rectangular dimensions, each having a single photomultiplier tube glued to the short side. The scintillators have a thickness of 23 mm matched to the photocathode diameter, a height of 34 mm and horizontal width of 60, 70 or 80 mm, with the shortest scintillators positioned closest to the beamline and the longest on the far end. A GAP-TPC (GTPC) between VTPC-1 and VTPC-2 improves the acceptance for high-momentum forward-going particles. The TPCs record the tracks and energy loss ($\mathrm{d}E/\mathrm{d}x$) of the charged particles produced in the collision. Their momentum vectors are calculated from the track parameters and the magnetic field.

The present analysis was performed on minimum bias proton-proton collision data at three beam momenta 158, 80 and 40 GeV/c. The recorded and selected event statistics are shown in Table 1. The difference between the two numbers is caused by the event selection cuts (see below).

A large sample of Monte Carlo (MC) events was generated in order to estimate the corrections for detector and analysis deficiencies. The MC samples contained 20 million $p + p$ events at each collision energy. These were generated using the Epos 1.99 model [23, 24] available within the Crmc 1.4 package [27]. The detector response was simulated using the Geant 3.21 package [28]. Event reconstruction was performed by the same NA61/SHINE software version as used for the treatment of experimental data. Two modifications were applied to the original Epos code: the natural width of the ϕ resonance was adjusted to its PDG value [29]; the branching ratio for the $\phi \to K^+K^-$ decay channel was set to 100 %

to increase the number of detectable ϕ decays. By virtue of the relatively small ϕ multiplicity, this latter change has no significant effect on the overall event characteristics and thus does not bias the obtained corrections. Epos was chosen as event generator, because other tested models performed worse in comparison with NA61/SHINE results on hadron production in hadron-hadron and hadron-nucleus interactions [21, 30–32].

Well studied cuts were applied to obtain a clean sample of inelastic $p + p$ events (see Ref. [22]). These include the requirements of the reconstruction of the interacting beam particle in the Beam Position Detectors and of the interaction point well inside the target vessel. Furthermore, events with a single, well measured positively charged track with absolute momentum close to the beam momentum were rejected. These are considered to be elastic events in which the beam proton scattered elastically into the acceptance of the TPCs. This rejection was needed only for the two lower beam momenta, because at 158 GeV/c the veto counter intercepted essentially all of the forward going protons from elastic $p+p$ interactions [22].

3 Analysis methodology

This section outlines the analysis procedure and describes the details of track selection, of ϕ signal extraction as well as the necessary corrections and systematic uncertainties. Since ϕ mesons cannot be detected directly, they are identified using the most frequent charged particle decay mode $\phi \rightarrow K^+K^-$. Their yield is obtained from the invariant mass distribution of pairs of oppositely charged particles assuming the kaon mass. Decays of ϕ mesons into K^+ and K^- manifest themselves as a resonance signal on a background of uncorrelated pairs and correlated pairs from decays of other unstable particles or resonances into oppositely charged particles. The number of uncorrelated pairs is significantly reduced, if only charged kaons are considered. Therefore kaon candidates are selected using the information about particle momenta and energy loss provided by the TPCs, as well as time-of-flight provided by the TOF-walls. The resulting invariant mass spectrum contains correlated K^+-K^- pairs, correlated pairs of charged particles with one or two wrong mass assignments, and uncorrelated pairs. The significance of the ϕ signal depends on the quality of the kaon identification, and the phase space distribution of the contributing particles. The number of ϕ mesons is determined by fitting suitable parametrizations of the signal and of the background to the invariant mass distributions.

The trajectories of the charged particles (the tracks) used in the invariant mass analysis are reconstructed using TPC data. The reconstructed tracks are subjected to quality checks to select particles produced in the primary interaction, to ensure good momentum resolution, and to reduce fakes. For a complete description of the track cuts see Ref. [33]. Their distance of closest approach to the interaction point (main vertex) must not exceed 4 cm in the bend plane and 2 cm in the plane spanned by the beam and magnetic field direction. A further criterion requires that the tracks consist of more than 30 clusters ('points'). This ensures reasonable $\mathrm{d}E/\mathrm{d}x$ resolution. In addition the number of clusters per track reconstructed in the magnetic field must be larger than 15 in the VTPCs or more than 4 in the GAP TPC. This ensures reasonable momentum determination accuracy.

The efficient selection of kaon candidates is of great importance for the ϕ resonance analysis. It is mainly based on the momentum and energy loss measurements along the trajectories of the charged particles in the TPCs. The correlation of both quantities for all accepted positively charged particles is shown in Fig. 2a in terms of their momenta and (truncated) mean energy losses $\mathrm{d}E/\mathrm{d}x$. Kaon candidates are selected by a momentum-dependent $\mathrm{d}E/\mathrm{d}x$ window around the expectation value. The size of this window was chosen such that the possible loss of kaons is small. This is achieved by selecting tracks with $\mathrm{d}E/\mathrm{d}x$ within ±5 %

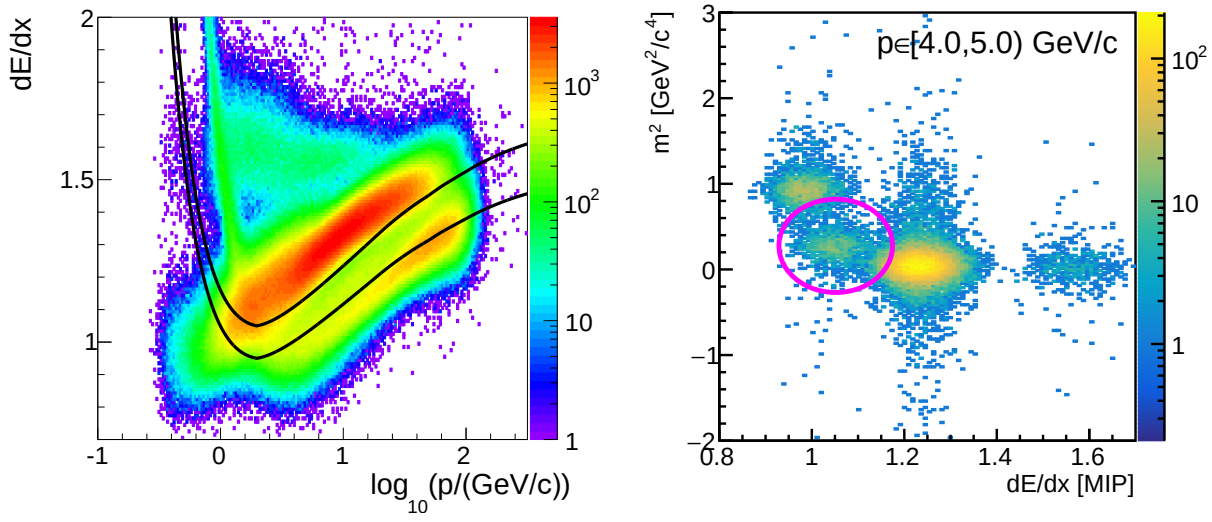

(a) (b)

Figure 2: Illustration of the kaon candidate selection. The data are from the 158 GeV/c run. The band between the two black curves in panel (a) is mainly populated by kaons and accepted in the analysis. Structures associated with pions and protons are visible above and below the band. (b) shows an example of how those particles are rejected which are with high probability not kaons by a cut in energy loss ($\mathrm{d}E/\mathrm{d}x$) and mass squared derived from TOF (outside of the pink circle).

of the nominal $\mathrm{d}E/\mathrm{d}x$ curve as given by the Bethe-Bloch formula. The experimental $\mathrm{d}E/\mathrm{d}x$ resolution is roughly 5%. The upper and lower limits of this cut are visualized as black lines in Fig. 2a. Particle time-of-flight information is available near midrapidity and is used to reject those particles which are not a charged kaon. An example is shown in Fig. 2b where particles outside the pink circle are rejected. The details of the time-of-flight measurement and calibration were described in Ref. [34].

The goal of the present analysis is to obtain the ϕ meson production yields in bins of rapidity y and transverse momentum p_{T}. This requires the study of the invariant mass distributions for each considered (y, p_{T}) bin. Several types of binning in rapidity and transverse momentum are used. They are all illustrated in Fig. 3. For comparison with other existing experimental data the results presented here are sometimes determined also in $(y, m_{\mathrm{T}} - m_0)$ bins, where m_0 is the rest mass of the ϕ meson.

The invariant mass spectrum of ϕ candidates in the (y, p_{T}) bin specified in Fig. 3d is shown in Fig. 4. The ϕ signal peaks around 1020 MeV/c^2 on a more or less structureless background. The signal is parametrized with a function which contains two components that take into account the natural shape of the resonance and its broadening due to the detector resolution. The first component is described by a relativistic Breit-Wigner function:

$$L(x; m_\phi, \Gamma) \propto \frac{x\Gamma_x(x)}{\left(x^2 - m_\phi^2\right)^2 + m_\phi^2 \Gamma_x^2(x)}, \tag{2a}$$

with

$$\Gamma_x(x) = 2\Gamma \left(\frac{q(x)}{q(m_\phi)}\right)^3 \frac{q^2(m_\phi)}{q^2(x) + q^2(m_\phi)}, \tag{2b}$$

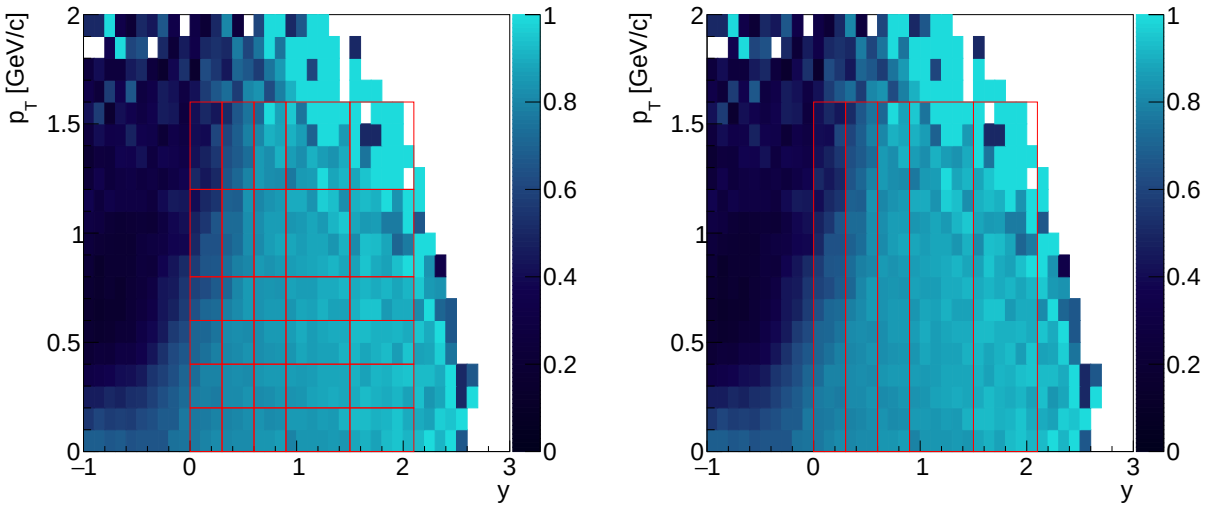

(a) 2D y, p_{T} binning

(b) 1D y binning

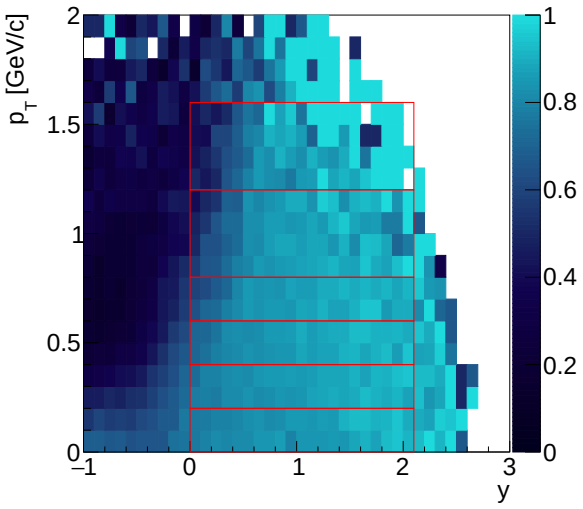

(c) 1D p_{T} binning

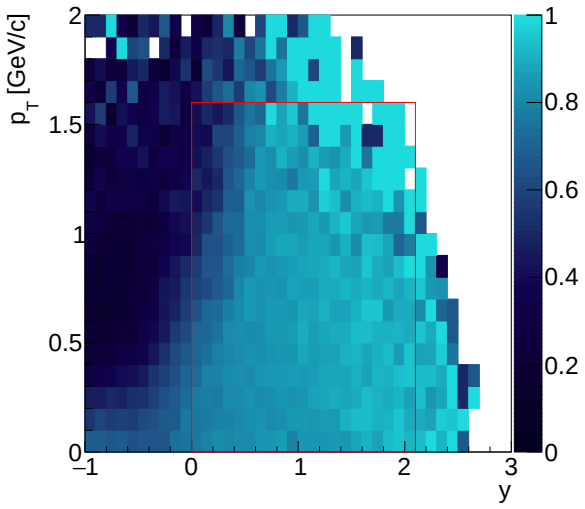

(d) broad binning

Figure 3: Binning types used in this analysis, overlaid on the ϕ registration probability obtained from simulations of inelastic p+p interactions at 158 GeV/c. Empty regions correspond to bins where probability calculation was not possible due to insufficient statistics of generated particles.

and

$$q(x) = \sqrt{\tfrac{1}{4}x^2 - m_K^2}\,, \tag{2c}$$

where m_ϕ is the peak position (expected to be equal, within uncertainties, to the mass of the ϕ meson), Γ is the natural width of the ϕ, and m_K is the kaon mass. This parametrization was adopted from Ref. [18] and first introduced in Ref. [35].

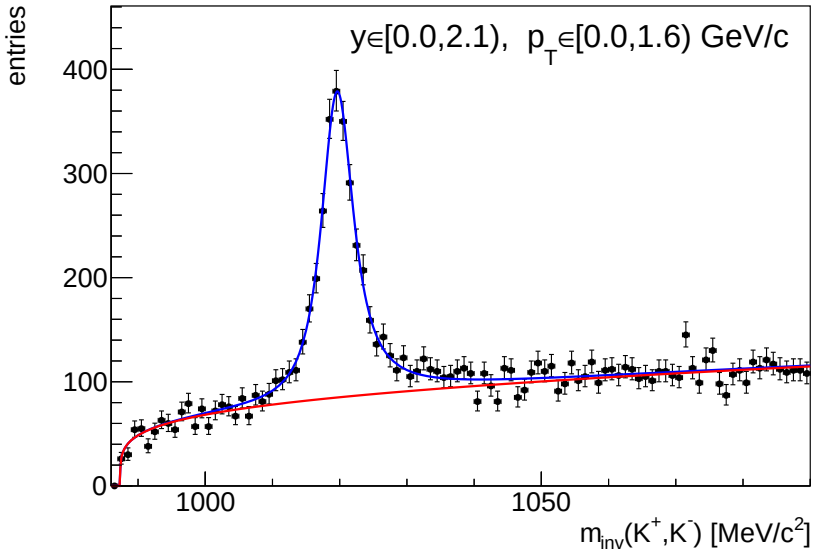

Figure 4: Example of a fitted invariant mass spectrum of kaon pair candidates in a large ϕ phase space region as defined in Fig. 3d, obtained for inelastic p+p interactions at 158 GeV/c. Both kaon candidates are subjected to the identification procedure. The signal shape parameters m_ϕ and σ resulting from this fit are used to constrain the fits in fine binned ϕ phase space. The blue curve represents the fitted function defined by Eq. (6), while the red curve represents the background component. Its shape is given by the ARGUS function. See the text for details.

The second component is described by the q-Gaussian function:

$$G(x;\sigma,q) \propto \left[1 + (q-1)\frac{x^2}{2\sigma^2}\right]^{-\frac{1}{q-1}}, \tag{3}$$

where σ is the width and q the shape parameter. The choice of this parametrization is discussed in Ref. [33]. As stated there, the parameter q is not fitted to data but fixed using a Monte Carlo study of the experimental invariant mass resolution. It no longer appears as a parameter of the function G.

The resulting resonance peak function is given by the convolution of Eqs. (2) and Eq. (3):

$$V(x;m_\phi,\sigma,\Gamma) = L * G = \int_{-\infty}^{+\infty} G(x';\sigma)L(x-x';m_\phi,\Gamma)\,\mathrm{d}x' \,. \tag{4}$$

In practice, it is not possible to simultaneously fit the two width parameters, σ and Γ. Therefore the Γ parameter is fixed to its PDG value and dropped from the list of fitted parameters in all further equations.

A reliable description of the background under the ϕ signal must take into account that the signal is close to the lower kinematical limit of the invariant mass given by the mass of two kaons. We use the ARGUS function [36] to describe the background under the ϕ signal. The function has two shape parameters and reads:

$$B(x;k,p) = \begin{cases} 0 & \text{for } x \le 2m_K \\ z(x)\cdot\left(1-\frac{z^2(x)}{x_{\max}^2}\right)^p \cdot \exp\left\{k\left(1-\frac{z^2(x)}{x_{\max}^2}\right)\right\} & \text{for } x > 2m_K \end{cases}, \tag{5a}$$

with

$$z(x) = 2m_K + x_{\max} - x\,, \tag{5b}$$

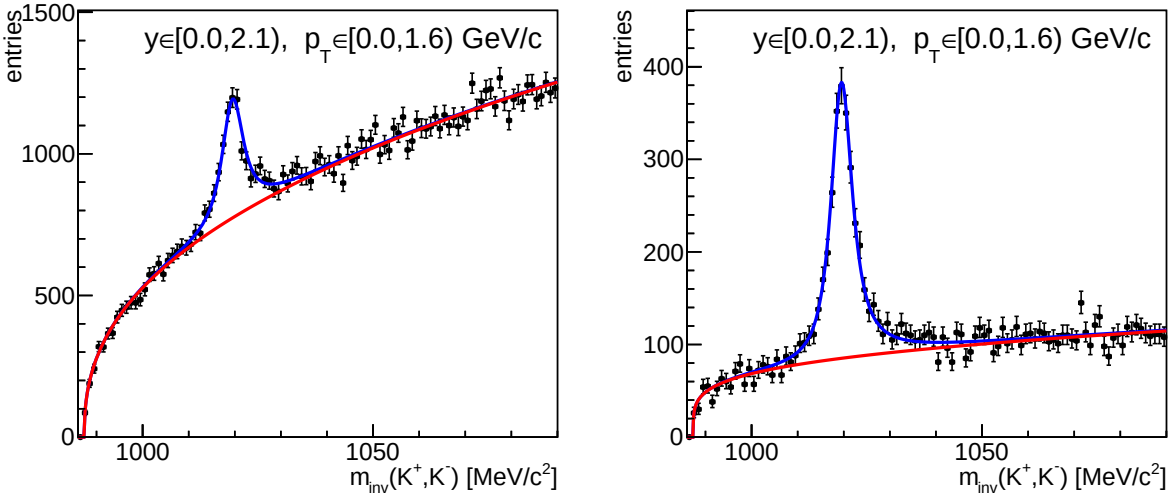

Figure 5: Illustration of a simultaneous tag-and-probe fit for the same data as shown in Fig. 4 with only one of the kaon candidates subjected to the particle identification conditions (left) and same data as Fig. 4 with both kaon candidates subjected to the PID procedures (right). Note that here the resonance signal parameters are kept fixed and the new parameter ε is introduced. The blue curves represent the fitting function defined by Eq. (8) and the red curves the background. See text for description of quoted parameters.

where k is a shape parameter corresponding to $-\frac{1}{2}\chi^2$ in the Wikipedia formula for the ARGUS distribution, p is the power as in the generalized ARGUS distribution, m_K is the kaon mass and $x_{\max}$ is the right boundary of the m_{inv} histogram. Note that in this parametrization, based on the class `RooArgusBG` from [37], k can be any real number. The complete function used to fit the invariant mass spectrum is shown as blue curve in Fig. 4. It is defined as:

$$f(m_{\text{inv}}) = N_{\text{p}} V(m_{\text{inv}}; m_\phi, \sigma) + N_{\text{bkg}} B(m_{\text{inv}}; k, p), \tag{6}$$

where $V(m_{\text{inv}}; m_\phi, \sigma)$ is given by Eq. (4) and $B(m_{\text{inv}}; k, p)$ by Eqs. (5). Both are normalised in such a way that N_{p} and N_{bkg} are the number of signal and background pairs in the mass distribution.

3.1 The tag-and-probe method

The procedure used to extract the ϕ yields follows the approach introduced by the LHCb [17] and ATLAS [16] collaborations. It is called the "tag-and-probe method" and automatically corrects for losses due to kaon candidate identification inefficiencies. The procedure uses two data samples which differ only in the particle identification conditions. Either both partners or at least one partner of the pair are required to fulfill the PID condition selecting a kaon candidate. The former requirement leads to the probe sample of particle pairs entering the invariant mass distribution (see Fig. 5). The tag sample is shown in the left panel of Fig. 5. The difference between the probe sample and the tag sample is a much better signal to background ratio in the former, because of the more complete PID information. The large increase of the background in the latter is predominantly caused by misidentified pions. This gives room for a signal from the decay of the $K^*(892)^0$ resonance visible as a bump above the background at about 1075 MeV/c^2.

The simultaneous description of the invariant mass distributions built from the tag and probe samples has a new parameter ε which is the efficiency of kaon selection (i.e. the probability that the kaon is accepted

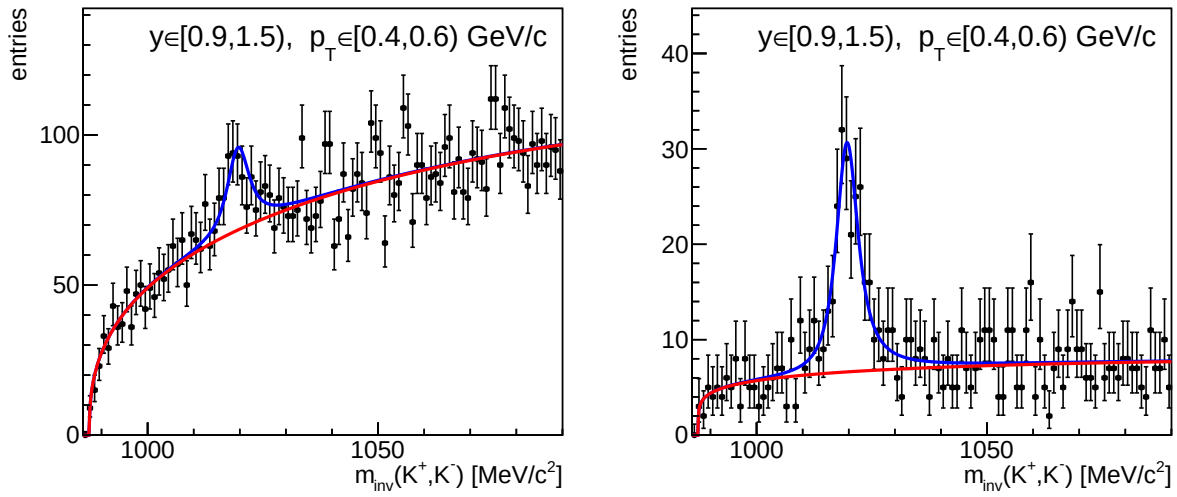

Figure 6: Example of a simultaneous tag-and-probe fit done in the final step of the fitting strategy to determine the raw ϕ yield for one of 2D phase space bins of the 158 GeV/c data. The tag (probe) sample is shown in the left (right) panel. The rapidity and p_{T} intervals are indicated in the figures.

by the PID cut). It correlates the total number of ϕ mesons (N_ϕ) in the event ensemble with the number of ϕ mesons in tag sample N_{t} and in the probe sample N_{p}. For the tag sample the correlation reads:

$$N_{\mathrm{t}}\big(N_\phi, \varepsilon\big) = N_\phi \varepsilon (2 - \varepsilon)\,, \tag{7a}$$

while that in the probe sample is

$$N_{\mathrm{p}}\big(N_\phi, \varepsilon\big) = N_\phi \varepsilon^2\,. \tag{7b}$$

The function used to fit simultaneously both the tag and the probe invariant mass distributions reads:

$$f(m_{\mathrm{inv}}) = \begin{cases} N_{\mathrm{t}}\big(N_\phi, \varepsilon\big) V(m_{\mathrm{inv}}; m_\phi, \sigma) + N_{\mathrm{bkg,t}} B_{\mathrm{t}}(m_{\mathrm{inv}}; k_{\mathrm{t}}, p_{\mathrm{t}}) & \text{for the tag} \\ N_{\mathrm{p}}\big(N_\phi, \varepsilon\big) V(m_{\mathrm{inv}}; m_\phi, \sigma) + N_{\mathrm{bkg,p}} B_{\mathrm{p}}(m_{\mathrm{inv}}; k_{\mathrm{p}}, p_{\mathrm{p}}) & \text{for the probe} \end{cases}, \tag{8}$$

where the quantities $V(m_{\mathrm{inv}}; m_\phi, \sigma)$ are given by Eq. (4), while $B_{\mathrm{t}}(m_{\mathrm{inv}}; k_{\mathrm{t}}, p_{\mathrm{t}})$ and $B_{\mathrm{p}}(m_{\mathrm{inv}}; k_{\mathrm{p}}, p_{\mathrm{p}})$ are the ARGUS functions (Eqs. (5)) describing the backgrounds for the tag and probe samples, respectively. All three expressions are normalised in such a way that the terms N_{t} and N_{p} defined by Eqs. (7) give the numbers of signal pairs in the tag and probe spectra, while $N_{\mathrm{bkg,t}}$ and $N_{\mathrm{bkg,p}}$ give the numbers of background pairs in the respective histograms. In total there are ten free parameters to be fitted to the data, four for the signal (N_ϕ, ε, m_ϕ, σ) and six for the background ($N_{\mathrm{bkg,t}}$, k_{t}, p_{t}, $N_{\mathrm{bkg,p}}$, k_{p}, p_{p}).

Note that N_ϕ should be understood as the number of ϕ mesons, the daughters of which pass all track cuts apart from the PID cut. This means that this number is still subject to corrections for various effects other than PID (like e.g. geometrical acceptance, reconstruction as well as trigger efficiency).

3.2 Fitting strategy

Due to limited statistics not all parameters of Eq. (8) discussed above can be fitted in each analysis bin separately. A three-step fitting strategy was developed instead. All the fits are extended binned log-likelihood fits (see e.g. Ref. [38]).

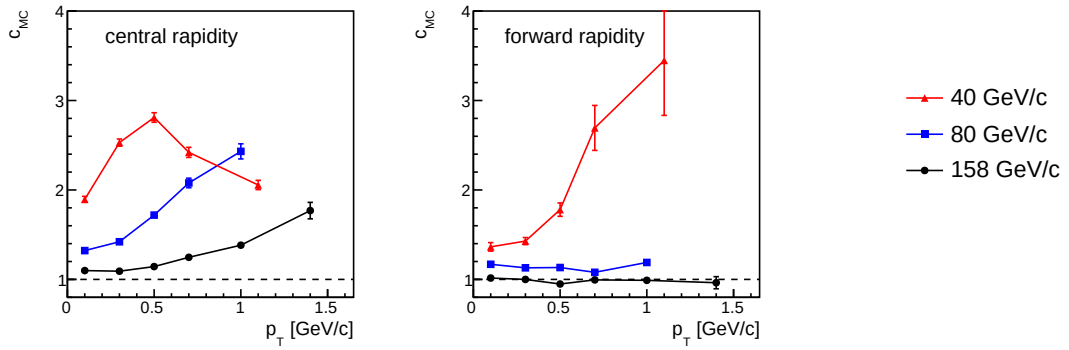

Figure 7: The Monte Carlo correction coefficient c_{MC} drawn as a function of transverse momentum for one central and one forward rapidity bin, at beam momenta of 40 GeV/c (red), 80 GeV/c (blue) and 158 GeV/c (black). The central rapidity bin (left) is always (0.0,0.3) while the forward rapidity bin (right) is (0.9,1.2) for 40 GeV/c beam momentum and (0.9,1.5) at other beam momenta.

In a first step precise values of signal shape parameters m_ϕ and σ are determined on a high statistics histogram which uses a large part of the covered phase space. The corresponding invariant mass distribution is shown in Fig. 4 together with the function defined by Eq. (6). The resulting values of m_ϕ and σ are fixed in further steps.

In a second step the values of the PID efficiency parameter ε are determined for use in step three. In this single differential analysis five bins in rapidity are used with an integration over a broad range in transverse momentum (Fig. 3b). In each bin of rapidity, a simultaneous tag-and-probe fit is performed using the function Eq. (8), with fixed signal shape parameters m_ϕ and σ. The resulting ε values vary from 0.61 ± 0.06 at low rapidities to 0.93 ± 0.06 at high rapidities. This procedure assumes that the kaon identification efficiency does not change significantly with p_{T} which has been demonstrated in Ref. [33].

Finally, in the third step of the strategy, simultaneous tag-and-probe fits are done in all selected rapidity and transverse momentum bins and provide the raw ϕ yields of the one-dimensional and two-dimensional analyses. Again the function Eq. (8) is employed, with fixed signal shape parameters m_ϕ and σ, and with ε determined as explained above. An example is shown in Fig. 6.

3.3 Corrections

The present analysis includes corrections for the branching ratio of the ϕ decay into K^+ K^- and the cut-off used in the integration of the resonance signal. A Monte Carlo-based procedure provides the corrections for losses due to the vertex cuts, geometrical acceptance of kaons coming from ϕ decays, the track reconstruction inefficiency including bin migration due to momentum resolution, and the event losses introduced by the minimum bias trigger.

The fully corrected double differential spectrum of the number of ϕ mesons per event is given by

$$\frac{\mathrm{d}^2 n}{\mathrm{d}p_{\mathrm{T}}\,\mathrm{d}y} = \frac{N_\phi}{N_{\mathrm{ev}}\,\Delta p_{\mathrm{T}}\,\Delta y} \times \frac{c_\infty c_{\mathrm{MC}}}{\mathcal{BR}(\phi \to K^+K^-)}, \tag{9}$$

where the first term is the normalized raw spectrum obtained in the analysis with the bin widths Δp_{T} and Δy; c_∞ is the correction due to the integration cut-off and of order of 6%. The $\mathcal{BR}(\phi \to K^+K^-)$ is taken from Ref. [29].

Table 2: Bin-independent systematic uncertainties. 'Total' is calculated by adding the contributions in quadrature.

	uncertainty value [%]		
Source	158 GeV/c	80 GeV/c	40 GeV/c
branching ratio	1	1	1
fitting constraints	2	3	4
ϕ signal	3	3	3
correction averaging	—	—	3
Total	6	7	8

The Monte Carlo correction factors c_{MC} in various (y, p_{T}) bins are shown in Fig. 7 as a function of the transverse momentum for one central and one forward bin in rapidity at three collision energies. The correction clearly depends on both y and p_{T}, and also on collision energy. The latter is not surprising as different beam energies mean different boosts of the emitted particles which cause different opening angles and thus increasing acceptance losses with decreasing energy. The correction coefficient can be both above and below unity. The latter is caused by trigger and vertex cut losses which both tend to eliminate low multiplicity $p + p$ events and to artificially enhance the measured ϕ yield. A complete description of the correction procedures with their uncertainties can be found in Ref. [33]. The systematic errors are addressed in the next paragraph.

The choice of the integration range used to obtain the ϕ yield from the signal parametrization curve has a negligible effect on the magnitude of the respective correction factor (1.06). Similarly, variations of the ϕ production model used in the Monte Carlo correction averaging in case of the single differential analysis does not change the results significantly. Bin-independent systematic uncertainties arise from the choice of the fitting constraints, the ϕ signal parametrization, and the correction averaging. They are listed in Table 2. The particle identification efficiencies which are determined by the tag and probe analysis may not be constant in the considered rapidity and transverse momentum bins. The resulting systematic uncertainties are due to shortcomings in the particle identification procedures which may generate systematic errors of the tag and probe analysis. The corresponding uncertainties can be read off the diagrams presented in Figs. 8 and 9. They stay well below the statistical errors which are added for comparison. Also shown are the systematic errors introduced by the event and track cuts which may occur, if the generated MC events do not precisely enough reproduce the experimental distributions of the cut variables. A further source of systematic uncertainty is the choice of the background function for the fit of the invariant mass distribution. The ϕ mass is near to the two-kaon mass threshold. The background at threshold may have (small) contributions of correlated kaons from f_0 or a_0 decays. Also at about 1075 MeV/c^2 possible correlated pairs of kaons and misidentified pions from the decay of the $K^*(892)^0$ resonance may appear, especially in the tag sample. To estimate the associated systematic uncertainty the fit range was varied and the resulting yield differences were used as one set of systematic errors. A second set was obtained by replacing the ARGUS function by a function consisting of templates of the combinatorial background (from event mixing), of $K^*(892)^0$ resonance decays, and of f_0- or a_0-like decays. The largest of the two estimates was taken bin-by-bin as the systematic error. The total systematic error is calculated by adding all contributions in quadrature and stays always below or close to the statistical error in Figs. 8 and 9.

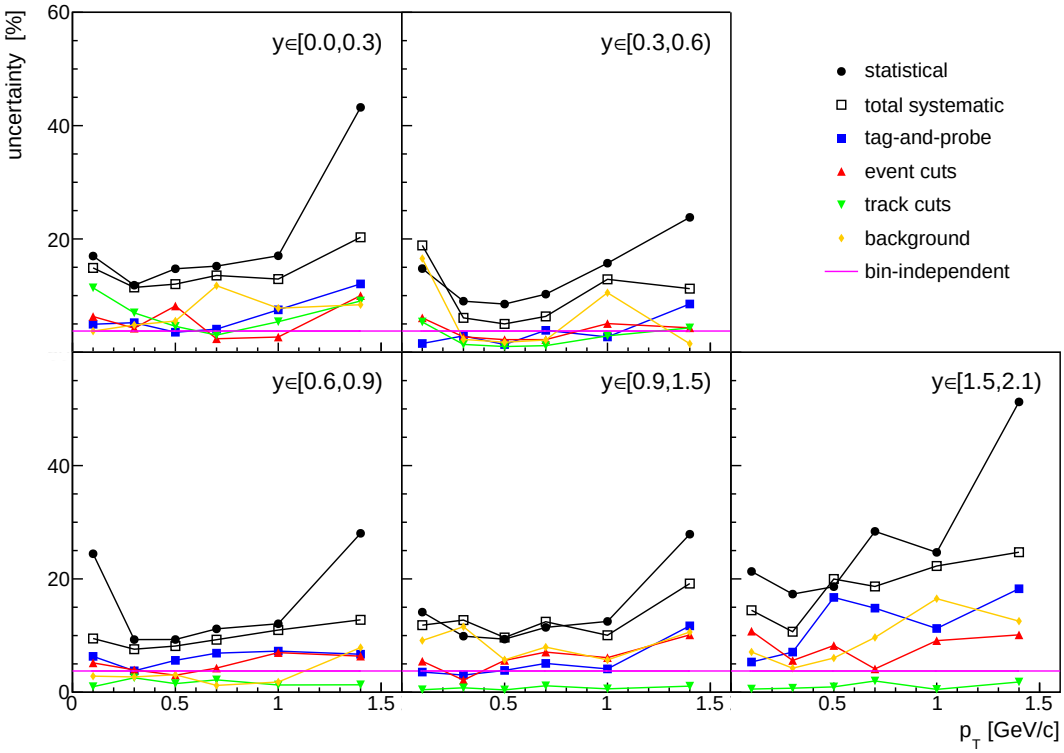

(a) 158 GeV/c

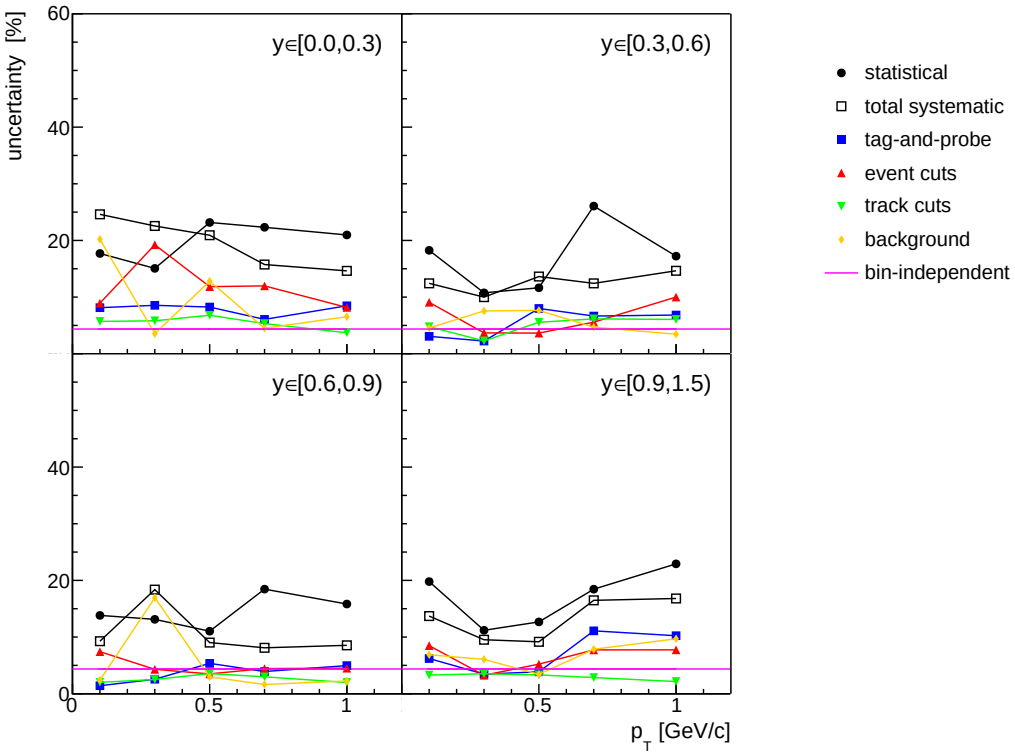

(b) 80 GeV/c

Figure 8: Comparison of statistical and systematic uncertainties for the double differential analysis of 158 GeV/c (a) and 80 GeV/c data (b). The p_{T} dependences are shown for different rapidity intervals. Total systematic uncertainty is calculated by adding contributions in quadrature.

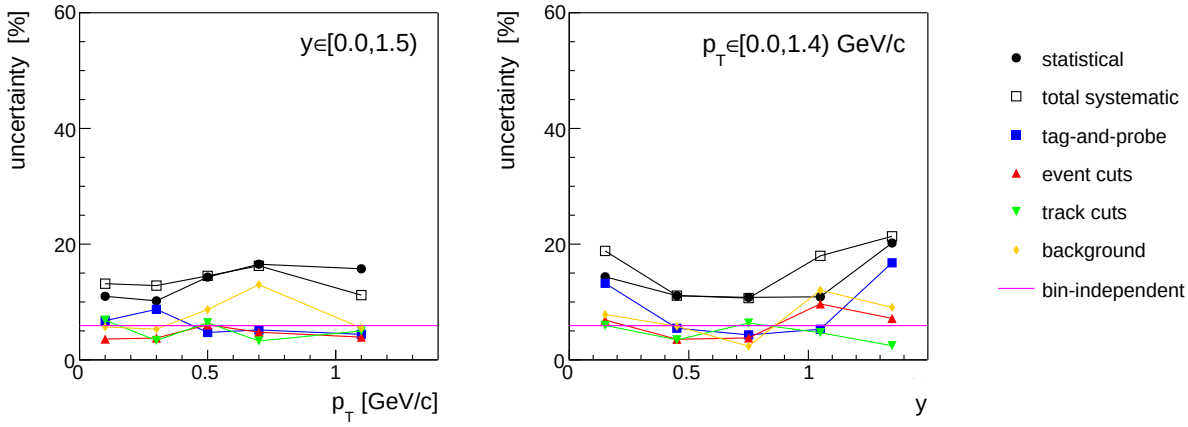

Figure 9: Comparison of statistical and systematic uncertainties for the single differential analysis of 40 GeV/c data. The p_{T} (left) and rapidity (right) dependences are shown for the indicated rapidity and p_{T} intervals. The total systematic uncertainties are calculated by adding the five contributions in quadrature.

4 Results

Yields of ϕ mesons have been determined as function of transverse momentum (up to 6 bins) and rapidity (up to 5 bins) in $p+p$ interactions at beam momenta of 158 GeV/c and 80 GeV/c. These are the first double differential measurements of ϕ production in proton-proton collisions at CERN SPS energies. Due to low statistics ϕ yields at 40 GeV/c have only been obtained as function of transverse momentum (5 bins) and rapidity (5 bins) (integrated over rapidity and transverse momentum, respectively).

The resulting transverse momentum spectra are shown in Fig. 10a for the 158 GeV/c, in Fig. 10b for the 80 GeV/c and Fig. 11 for the 40 GeV/c data. If the yields, divided by the transverse mass (m_{T}), are plotted as function of $m_{\mathrm{T}} - m_0$ instead exponential shapes emerge as shown for the midrapidity bins in Fig. 12a and Fig. 12b. This suggests to fit the transverse momenta (mass) spectra with the function defined in Eq. (10)

$$f(p_{\mathrm{T}}) = A \times p_{\mathrm{T}} \exp\left(-\frac{m_{\mathrm{T}}}{T}\right), \tag{10}$$

to characterize the shape of the spectra by a single slope parameter T and to estimate the yield outside of the acceptance (at high transverse momenta). For 158 GeV/c and 40 GeV/c these contributions are below 1 % for all rapidity bins, while for 80 GeV/c they are of the order of 1 % to 4 %. The function $f(p_{\mathrm{T}})$ describes the experimental data within errors in all rapidity bins. The rapidity dependence of the slope parameter T, often called effective temperature, is given in Fig. 13a (left) for the 158 GeV/c and in Fig. 13b (left) for the 80 GeV/c data. Rapidity yields are obtained by summing the content of the corresponding p_{T} spectra and adding the corrections for the unmeasured regions. The resulting rapidity spectra (in the centre-of-mass) are shown in Fig. 14a (158 GeV/c), Fig. 14b (80 GeV/c), and Fig. 14c (40 GeV/c) in the forward hemisphere. Their shapes can be approximated by Gaussian distributions. The corresponding fits with

$$g(y) = A \times \exp\left(-\frac{y^2}{2\sigma_y^2}\right), \tag{11}$$

provide width parameters σ_y for each p_{T} bin which are shown in Fig. 13 (right).

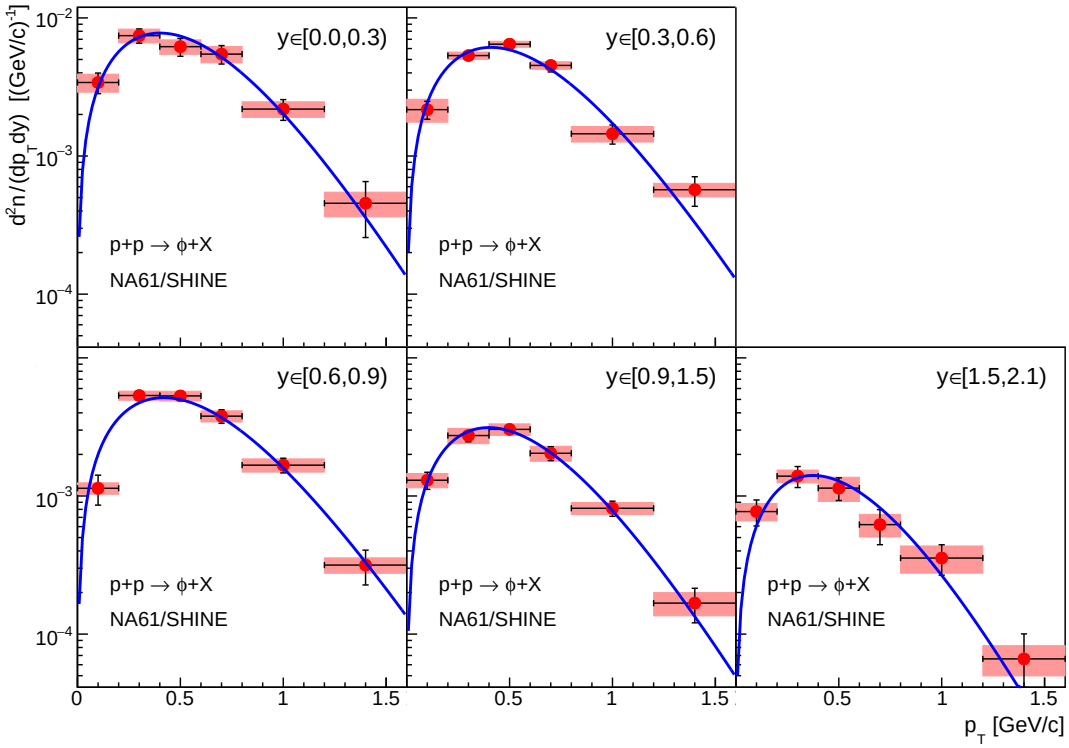

(a) 158 GeV/c

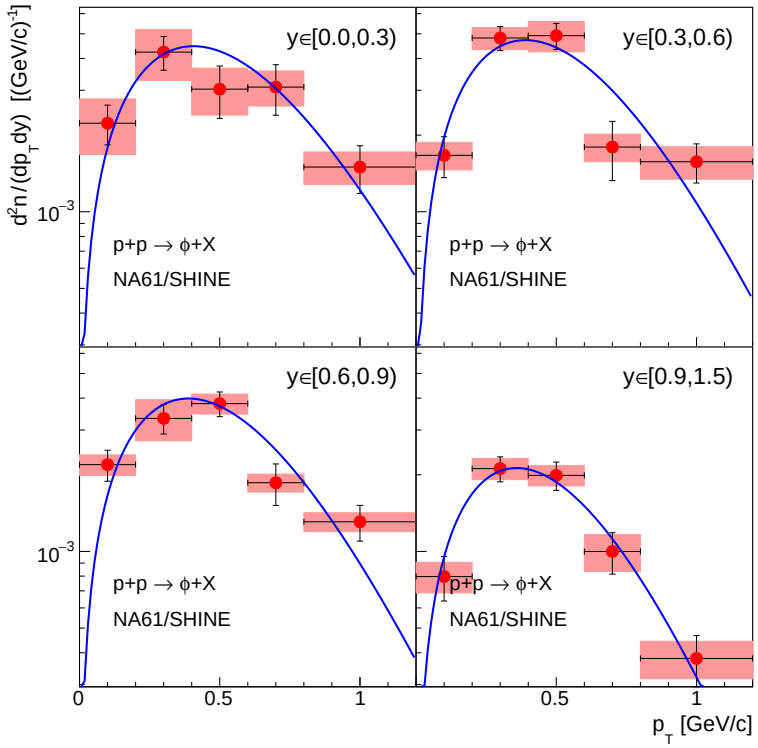

(b) 80 GeV/c

Figure 10: Transverse momentum spectra in 6 rapidity bins for 158 GeV/c and 5 rapidity bins for 80 GeV/c data with statistical errors (vertical bars) and systematic errors (red shaded bands). The horizontal bars indicate the bin size. Curves are fits of function Eq. (10).

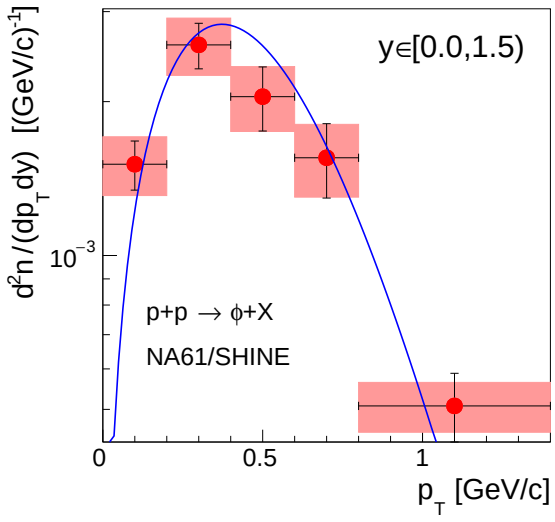

Figure 11: Transverse momentum spectrum integrated over rapidity for 40 GeV/c data with statistical errors (vertical bars) and systematic errors (red shaded bands). The horizontal bars indicate the bin size. Solid blue curve is a fit of the function defined in Eq. (10).

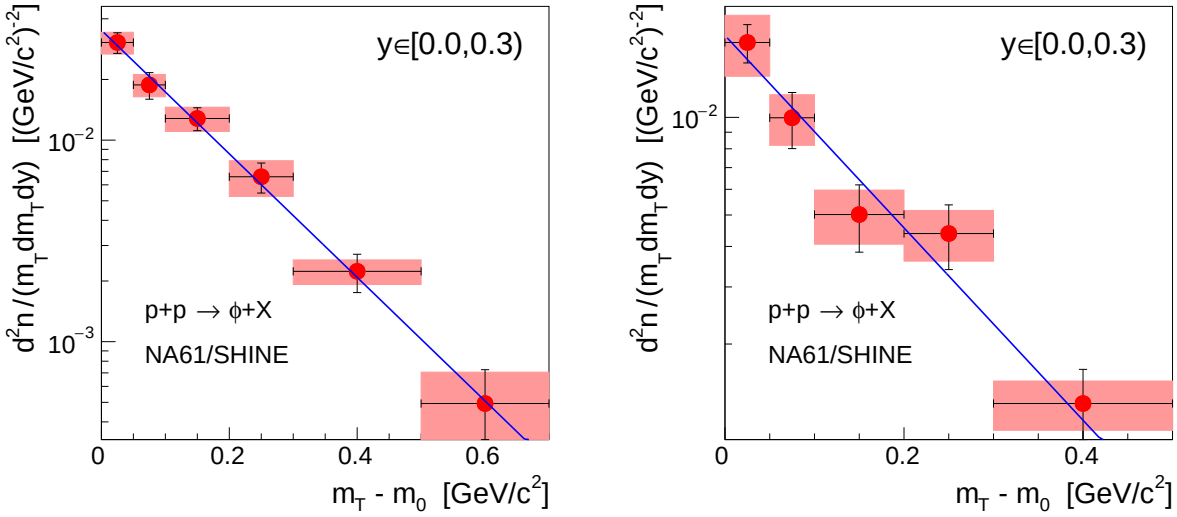

(a) 158 GeV/c (b) 80 GeV/c

Figure 12: Transverse mass spectra at midrapidity for 158 GeV/c (left) and 80 GeV/c (right). The straight lines are the fits of Eq. (10) to the data points.

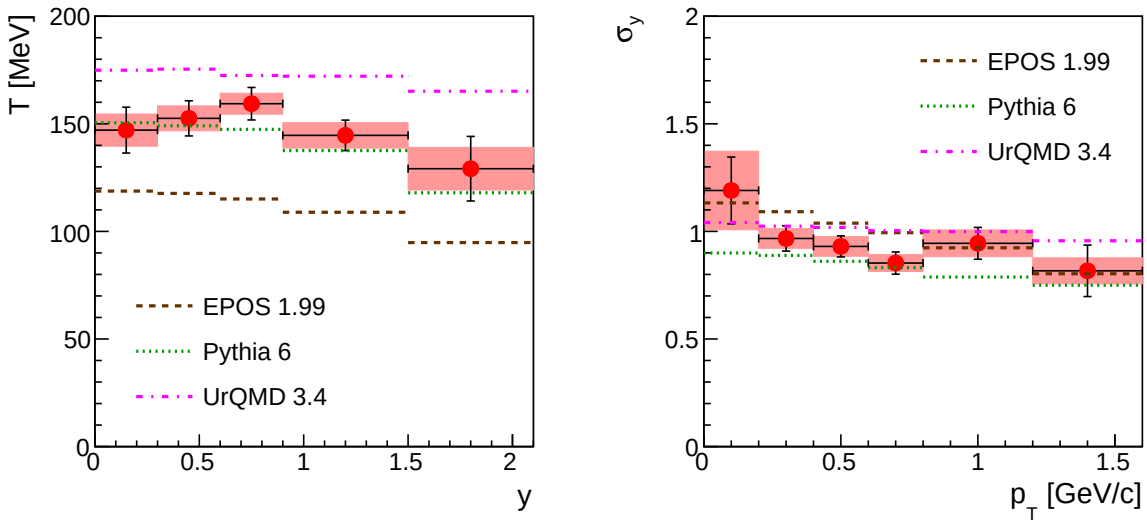

(a) 158 GeV/c

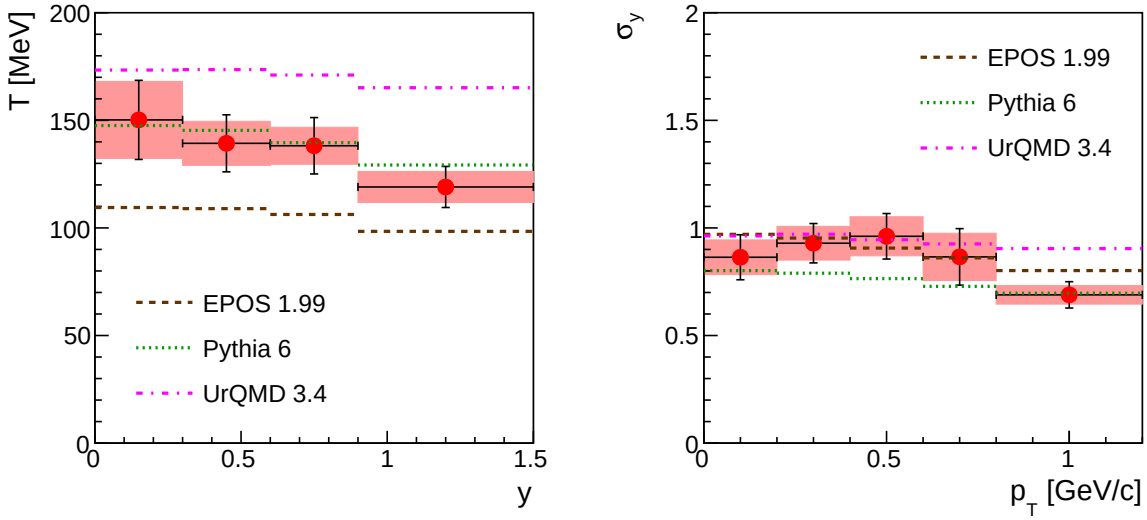

(b) 80 GeV/c

Figure 13: Dependence of the slope parameter T on rapidity (left) and the width σ_y of the rapidity distributions on p_T (right) for 158 GeV/c and 80 GeV/c data with statistical errors (vertical bars) and systematic errors (red bands). The horizontal bars indicate the bin size.

Total ϕ yields ($\langle\phi\rangle$) are obtained by summing the content of the rapidity spectra and adding a correction for the extrapolation into the unmeasured beam and target rapidity regions, which is obtained from the Gaussian fits. The unmeasured tail contributions to $\langle\phi\rangle$ are about 3 % for 158 GeV/c, 7 % for 80 GeV/c, and 5 % for 40 GeV/c. The results for $\langle\phi\rangle$, the width parameters σ_y and the midrapidity yield $\frac{dn}{dy}(y = 0)$ are listed in Table 3.

The ϕ multiplicity at 158 GeV/c reported here ($(12.56 \pm 0.33) \times 10^{-3}$) is in good agreement with the result quoted in Ref. [10] ($(12.0 \pm 1.5) \times 10^{-3}$). The latter is more than two times less accurate, mainly because

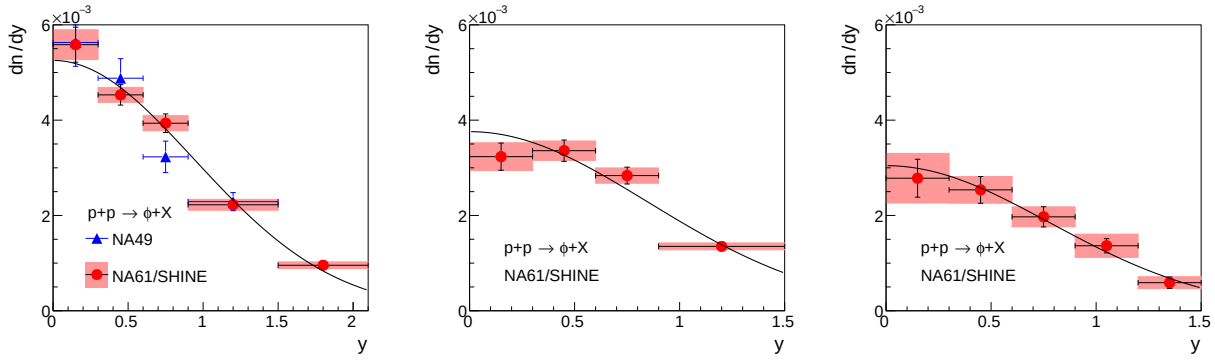

(a) 158 GeV/c (b) 80 GeV/c (c) 40 GeV/c

Figure 14: Rapidity spectra for 158 GeV/c, 80 GeV/c, and 40 GeV/c data with statistical errors (vertical bars) and systematic errors (red bands). The horizontal bars indicate the bin size. NA49 points (triangles) come from Ref. [10]. Solid curves are Gaussian fits (Eq. (11))

Table 3: Parameters deduced from rapidity distributions for all analysed beam momenta. The first uncertainty is statistical, the second one systematic.

p_{beam} [GeV/c]	σ_y	$\langle\phi\rangle$ [10^{-3}]	$\frac{dn}{dy}(y=0)$ [10^{-3}]	χ^2/ndf
158	$0.938 \pm 0.027 \pm 0.023$	$12.56 \pm 0.33 \pm 0.32$	$5.25 \pm 0.19 \pm 0.15$	0.94
80	$0.850 \pm 0.040 \pm 0.033$	$7.89 \pm 0.29 \pm 0.39$	$3.76 \pm 0.20 \pm 0.19$	1.73
40	$0.780 \pm 0.047 \pm 0.053$	$5.87 \pm 0.35 \pm 0.44$	$3.05 \pm 0.25 \pm 0.28$	0.27

of smaller rapidity coverage and the resulting large uncertainty of the extrapolation in rapidity. The NA61/SHINE result for the σ_y parameter (0.938 ± 0.027) also agrees with the NA49 finding of 0.89 ± 0.06 [10] within quoted uncertainties. In the present analysis the slope parameter T of the transverse momentum distribution was determined in the same phase bin as used by the NA49 collaboration and found at (146 ± 5) GeV within errors compatible with the NA49 measurement of (169 ± 17) GeV.

The NA61/SHINE results are now compared to three microscopic models. These are Epos 1.99 [23, 24] and Pythia 6.4.28 [42] from the Crmc 1.6.0 package [27] and UrQMD 3.4 [25, 26]. In Epos the ϕ width had to be adjusted to the PDG value. In case of Pythia, the main Perugia 2011 tune 350 [43] is used. The results of the model calculations on p_{T} and rapidity spectra are compared to the measurements in Fig. 13. Pythia reproduces the shapes of the p_{T} spectra quite well, while UrQMD produces slightly harder and Epos slightly softer spectra. This applies to both data sets 158 GeV/c and 80 GeV/c. The widths of the rapidity distributions are reproduced by the models within the systematic errors.

Figure 15a presents ratios of total yields of ϕ mesons to mean total yields of pions in $p+p$ and central Pb + Pb [18] collisions as a function of energy per nucleon pair. Mean total yields for pions are calculated as in Ref. [18] :

$$\langle\pi\rangle = \frac{3}{2}(\langle\pi^+\rangle + \langle\pi^-\rangle)\,. \tag{12}$$

The results confirm the enhancement of ϕ production (normalized to pions) in the SPS energy range. This enhancement can be quantified by the double ratio (see Fig. 15b):

$$\text{double ratio}\,(\langle\phi\rangle/\langle\pi\rangle) = \frac{(\langle\phi\rangle/\langle\pi\rangle)_{\text{Pb + Pb}}}{(\langle\phi\rangle/\langle\pi\rangle)_{p+p}}\,, \tag{13}$$

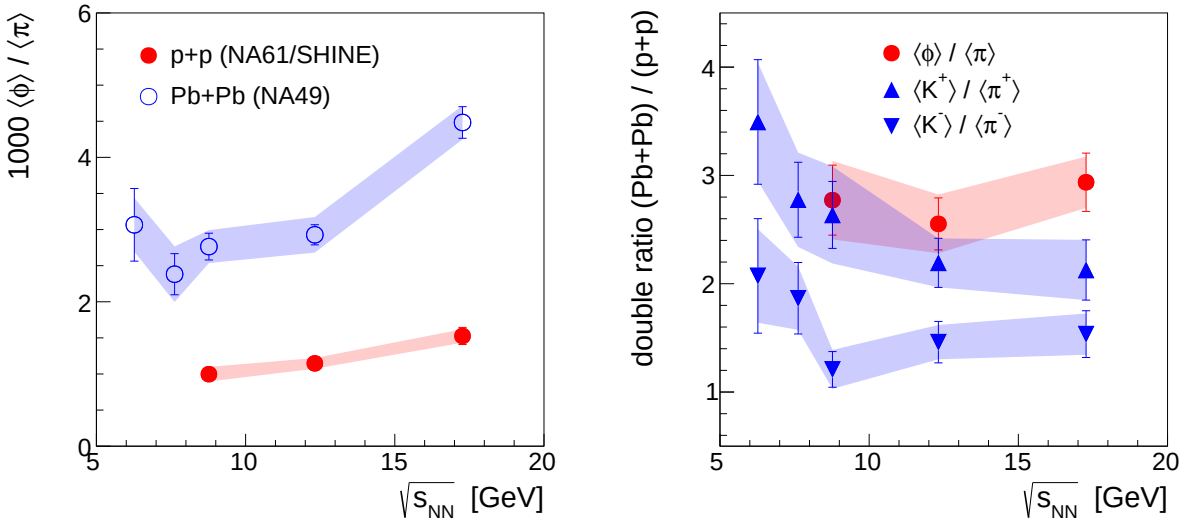

(a) (b)

Figure 15: Energy dependence of (a) ratios of total yields of ϕ mesons to mean total yields for pions (Eq. (12)) in $p+p$ and Pb+Pb, (b) double ratios (see text). Full red circles correspond to results of this analysis, Pb + Pb data come from NA49 [18, 39, 40], while $p+p$ kaon and pion data are taken from Ref. [41]. Possible correlations of uncertainties of yields within the same reaction are neglected. This may lead to a slight overestimation of the indicated uncertainties.

Clearly ϕ production is enhanced roughly threefold for all 3 measured energies. This was already observed in Ref. [18], in which a parametrization proposed in Ref. [44] of the ϕ production cross-section had been used as reference instead of experimental $p + p$ data.

The strangeness enhancement of ϕ mesons can be compared to that of charged kaons relative to charged pions (see Fig. 15b). It is systematically larger for ϕ mesons than for kaons, being however comparable to that for positive kaons.

Next the excitation function of ϕ meson production will be discussed. Figure 16 shows the energy dependence of total and midrapidity yields of ϕ mesons produced in $p + p$ collisions. For CERN SPS and ISR energies total inclusive cross-sections are given in Refs. [6–10]. They are converted into multiplicities for Figure 16a according to Eq. (1). At RHIC and LHC only midrapidity yields are measured [12, 14, 15]. The corresponding excitation function is shown in Figure 16b. Wherever systematic uncertainties of world data are available, they are summed quadratically with statistical uncertainties for brevity of presentation.

Straight lines are fitted to the data points in Fig. 16a assuming proportionality between the total energy available for production and the number of produced ϕ mesons. All measurements, i.e. world data and those from this analysis, are used in the fit. The resulting straight (red) line describes well the data in the considered energy range.

For midrapidity yields no well-motivated parameterisation of $\sqrt{s_{NN}}$ dependence exists. For simplicity the red dashed line in Fig. 16b corresponds to the function

$$f\left(\sqrt{s_{NN}}\right) = a \log_{10}\left(\sqrt{s_{NN}}/b\right), \tag{14}$$

which is a guess and happens to describe well the data points.

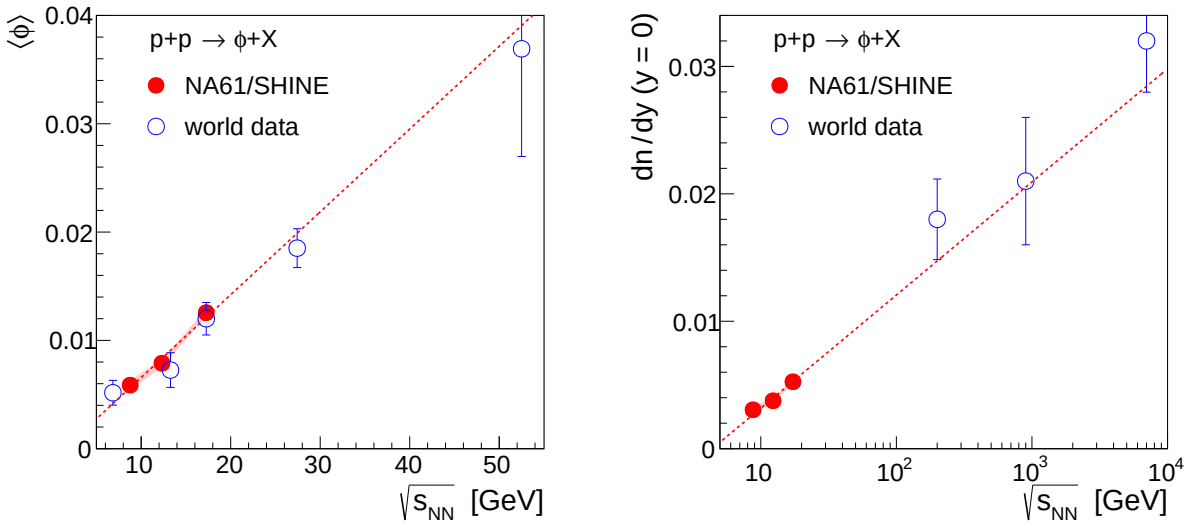

(a) (b)

Figure 16: Energy dependence of (a) total yields and (b) midrapidity yields of ϕ mesons in $p + p$ collisions. World data on total yields come from Refs. [6–10], while on midrapidity yields come from Refs. [12, 14, 15]. Red dashed lines are fits to guide the eye (see text).

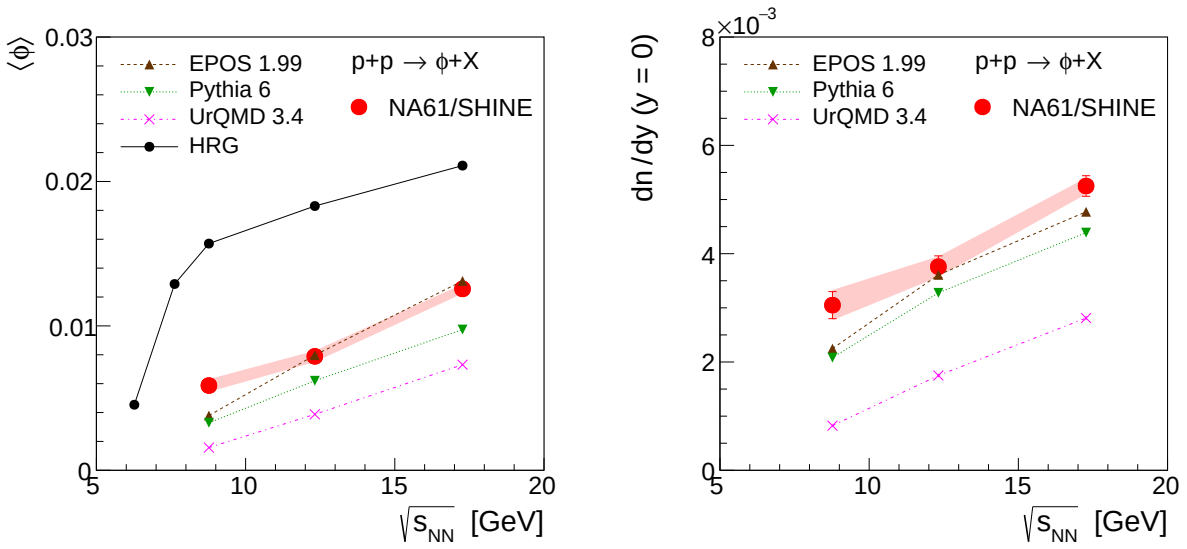

(a) (b)

Figure 17: Energy dependence of (a) total yields and (b) midrapidity yields of ϕ mesons in $p + p$ collisions at SPS energies. Also shown are the results of microscopic model calculations (Epos, Pythia, UrQMD) as well as the hadron resonance gas model (HRG).

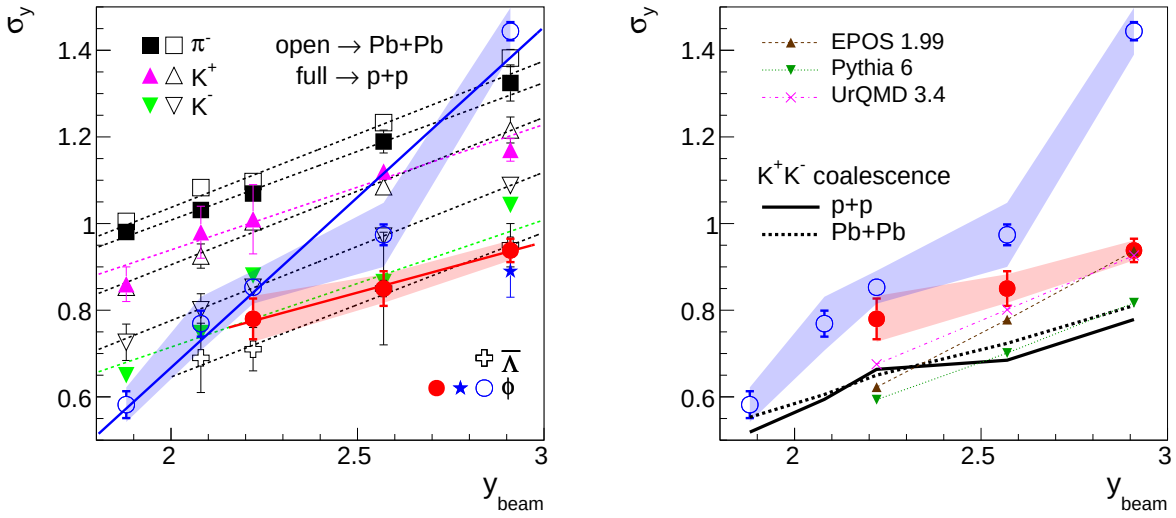

(a) (b)

Figure 18: (a) Widths of rapidity distributions of various particles in $p + p$ (full symbols) and central Pb + Pb collisions (open symbols) as a function of beam rapidity. Full red circles are results of this analysis, the star is the $p + p$ NA49 measurement [10], other $p + p$ points come from NA61/SHINE [22, 41], while the Pb + Pb points from NA49 [18, 39, 40, 45]. Lines are fitted to points to guide the eye. (b) Comparison of widths for ϕ mesons with expectations from kaon coalescence (see text) and models.

While Figure 16 covers the energy range up to LHC energies Figure 17 zooms in on the SPS energy range for the comparison to model calculations. One observes that the slope of the excitation function is reproduced by Pythia, UrQMD, and Epos within statistical and systematic uncertainties for both the total and mid-rapidity yields. The yields, however are off by factors of 0.25 and 0.7 for Pythia/Epos and UrQMD, respectively. The hadron gas model (HRG [1]) overpredicts the total yields by roughly a factor of two.

The last paragraph of this section addresses the so far not explained exceptional role which the ϕ meson plays when considering the widths of the rapidity distributions (σ_y) of produced particles as function of energy put forward by the NA49 collaboration [18]. Except for the ϕ these widths increase approximately linearly with beam rapidity, at the same rate and irrespective of the colliding system. Figure 18a shows the widths of the rapidity distributions of ϕ mesons and various other produced particles in $p + p$ and central Pb + Pb collisions as a function of beam rapidity in the centre-of-mass frame. The corresponding figure in Ref. [18] has been complemented by the NA61/SHINE results on π^- [22] and K^+,K^- in $p + p$ collisions. The σ_y of K^+ and K^- were calculated from the distributions given in Ref. [41]. The excitation function of σ_y for the ϕ meson in Pb + Pb collisions is significantly steeper than the one of the other particles. The peculiarity of this result is emphasized by the new NA61/SHINE $p + p$ data: the ϕ data points suggest that it is not the ϕ meson which is peculiar in itself, it rather is something specific to ϕ meson production in the heavy Pb + Pb system. Kaon coalescence is a possible source of ϕ mesons in the final state. It correlates σ_y of ϕ with σ_y of kaons. Thus one can calculate σ_y of ϕ from σ_y of kaons in $p + p$ and Pb + Pb using the method described in Ref. [18]. The result is shown as thick black lines for $p + p$ (solid) and Pb + Pb (dotted) in Fig. 18b together with the experimental data. The difference between the coalescence expectations and the actual measurements is much smaller for $p + p$ than for Pb + Pb data points.

5 Summary and conclusions

Spectra and multiplicities of ϕ mesons produced in inelastic p+p interactions were measured with the NA61/SHINE spectrometer at beam momenta 40 , 80 , 158 GeV/c at the CERN SPS. The tag-and-probe method, adapted from LHC analyses, was used to analyze the K^+- K^- invariant mass distributions. For the 158 GeV/c and 80 GeV/c data sets the analysis was done double differentially yielding spectra of rapidity and transverse momentum. The limited number of ϕ candidates for 40 GeV/c allowed only for a single differential analysis resulting in transverse momentum and rapidity spectra integrated over rapidity and transverse momentum, respectively. The statistical errors are larger than the systematic uncertainties for all energies. While each of the considered microscopic models reproduces the shape of either the transverse momentum or the rapidity spectra, none describes both consistently.

NA61/SHINE results on ϕ production in $p + p$ collisions are the elementary reference for the study of collective effects in Pb + Pb data [18]. They emphasize the intriguing energy dependence of σ_y of the ϕ meson in central Pb + Pb collisons. The widths of rapidity spectra in $p + p$ and Pb + Pb collisions are systematically larger than expected from the hypothesis that ϕ mesons are predominantly produced through kaon coalescence. Kaon coalescence can still be the most important mechanism in $p + p$ interactions, however in Pb + Pb collisions a new production process for ϕ mesons seems to become important at higher energies, which is not present in pion, kaon, and anti-Lambda production. Our findings at 158 GeV/c agree with previously published results from the NA49 collaboration [10] within quoted uncertainties. The latter are almost 3 times smaller in the NA61/SHINE than in the NA49 data. Neither total yields nor spectra on ϕ production in $p + p$ interactions have previously been published at beam energies of 40 GeV/c and 80 GeV/c.

Our results confirm that the excitation function of ϕ multiplicity is almost perfectly linear in $p + p$ interactions. In the low energy regime neither the three microscopic models, Ref. [23–26, 42] nor the statistical hadron gas model [1] can reproduce the experimmental excitation function quantitatively, the precision of which was increased significantly by the NA61/SHINE results.

Acknowledgments

We would like to thank the CERN EP, BE and EN Departments for the strong support of NA61/SHINE.

This work was supported by the Hungarian Scientific Research Fund (grant NKFIH 123842/123959), the Polish Ministry of Science and Higher Education (grants 667/N-CERN/2010/0, NN 202 48 4339 and NN 202 23 1837), the National Science Centre Poland (grants 2011/03/N/ST2/03691, 2013/11/N/ST2/03879, 2014/13/N/ST2/02565, 2014/14/E/ST2/00018, 2014/15/B/ST2/02537, 2015/18/M/ST2/00125, 2015/19/N/ST2/01689, 2016/23/B/ST2/00692, 2017/25/N/ST2/02575, 2018/30/A/ST2/00226), the Russian Science Foundation, grant 16-12-10176, the Russian Academy of Science and the Russian Foundation for Basic Research (grants 08-02-00018, 09-02-00664 and 12-02-91503-CERN), the Ministry of Science and Education of the Russian Federation, grant No. 3.3380.2017/4.6, the National Research Nuclear University MEPhI in the framework of the Russian Academic Excellence Project (contract No. 02.a03.21.0005, 27.08.2013), the Ministry of Education, Culture, Sports, Science and Technology, Japan, Grant-in-Aid for Scientific Research (grants 18071005, 19034011, 19740162, 20740160 and 20039012), the German Research Foundation (grant GA 1480/8-1), the Bulgarian Nuclear Regulatory Agency and the Joint Institute for Nuclear Research, Dubna (bilateral contract No. 4799-1-18/20), Bulgarian National

Science Fund (grant DN08/11), Ministry of Education and Science of the Republic of Serbia (grant OI171002), Swiss Nationalfonds Foundation (grant 200020117913/1), ETH Research Grant TH-01 07-3 and the U.S. Department of Energy.

References

[1] V. Vovchenko, V. V. Begun, and M. I. Gorenstein *Phys. Rev.* **C93** (2016) 064906.

[2] T. Sjostrand, S. Ask, J. R. Christiansen, R. Corke, N. Desai, *et al. Comput.Phys.Commun.* **191** (2015) 159.

[3] S. Roesler, R. Engel, and J. Ranft, "The Monte Carlo event generator DPMJET-III," in *Proc. MC2000*, pp. 1033–1038. 2000.

[4] B. Nilsson-Almqvist and E. Stenlund *Comput. Phys. Commun.* **43** (1987) 387.

[5] M. Gazdzicki, M. Gorenstein, and P. Seyboth *Acta Phys. Polon. B* **42** (2011) 307.

[6] V. Blobel *et al. Phys. Lett. B* **59** (1975) 88.

[7] C. Daum *et al.*, [ACCMOR Collab.] *Nucl. Phys. B* **186** (1981) 205.

[8] D. Drijard *et al. Z. Phys. C* **9** (1981) 293.

[9] M. Aguilar-Benitez *et al.*, [LEBC-EHS Collab.] *Z. Phys. C* **50** (1991) 405.

[10] S. Afanasiev *et al.*, [NA49 Collab.] *Phys. Lett. B* **491** (2000) 59.

[11] Y. Maeda *et al. Phys. Rev. C* **77** (2008) 015204.

[12] B. I. Abelev *et al.*, [STAR Collab.] *Phys. Rev. C* **79** (2009) 064903.

[13] M. Naglis *et al.*, [PHENIX Collab.] *Nucl. Phys. A* **830** (2009) 757c.

[14] K. Aamodt *et al.*, [ALICE Collab.] *Eur. Phys. J. C* **71** (2011) 1594.

[15] B. Abelev *et al.*, [ALICE Collab.] *Eur. Phys. J. C* **72** (2012) 2183.

[16] G. Aad *et al.*, [ATLAS Collab.] *Eur. Phys. J. C* **74** (2014) 2895.

[17] R. Aaij *et al.*, [LHCb Collab.] *Phys. Lett. B* **703** (2011) 267.

[18] C. Alt *et al.*, [NA49 Collab.] *Phys. Rev. C* **78** (2008) 044907.

[19] "Pdg tables on total and elastic cross sections as a function of energy.". http://pdg.lbl.gov/2015/hadronic-xsections/hadron.html.

[20] N. Abgrall *et al.*, [NA61/SHINE Collab.] *JINST* **9** (2014) P06005.

[21] N. Abgrall *et al.*, [NA61/SHINE Collab.] *Phys. Rev. C* **84** (2011) 034604.

[22] N. Abgrall *et al.*, [NA61/SHINE Collab.] *Eur. Phys. J. C* **74** (2014) 2794.

[23] K. Werner, F. Liu, and T. Pierog *Phys. Rev. C* **74** (2006) 044902.

[24] T. Pierog and K. Werner *Nucl. Phys. B (Proc. Suppl.)* **196** (2009) 102.

[25] S. Bass *et al. Prog. Part. Nucl. Phys.* **41** (1998) 255.

[26] M. Bleicher *et al. J. Phys. G* **25** (1999) 1859.

[27] C. Baus, T. Pierog, and R. Ulrich, "CRMC (Cosmic Ray Monte Carlo package).". https://web.ikp.kit.edu/rulrich/crmc.html.

[28] R. Brun, F. Carminati, and S. Giani, "GEANT Detector Description and Simulation Tool.". CERN Program Library Long Writeup W5013.

[29] K. Olive *et al.*, [Particle Data Group Collab.] *Chin. Phys. C* **38** (2014) 090001.

[30] A. Ilnicka, "Comparison of hadron production in Monte-Carlo models and experimental data in p+p interactions at the SPS energies," Master's thesis, University of Warsaw, 2013. https://edms.cern.ch/document/1319366.

[31] M. Unger for the NA61/SHINE Collaboration *PoS* **ICHEP 2010** (2010) 449.

[32] M. Unger for the NA61/SHINE Collaboration *EPJ Web Conf.* **52** (2013) 01009.

[33] A. Marcinek, *ϕ meson production in proton-proton collisions in the NA61/SHINE experiment at CERN SPS*. PhD thesis, Jagiellonian University, Kraków, 2016. https://edms.cern.ch/file/1736151/1/Antoni_Marcinek_PhD.pdf.

[34] A. Aduszkiewicz *et al.*, [NA61/SHINE Collab.] *Eur. Phys. J.* **C77** no. 10, (2017) 671.

[35] J. D. Jackson *Nuovo Cimento* **34** (1964) 1644.

[36] H. Albrecht, [ARGUS Collab.] *Z.Phys.C* **48** (1990) 543.

[37] W. Verkerke and D. Kirkby, "The RooFit Toolkit for Data Modeling.". http://root.cern.ch/drupal/content/roofit.

[38] G. Cowan, *Statistical Data Analysis*. Oxford University Press, Oxford, 1998.

[39] S. V. Afanasiev *et al.*, [NA49 Collab.] *Phys. Rev. C* **66** (2002) 054902.

[40] C. Alt *et al.*, [NA49 Collab.] *Phys. Rev. C* **77** (2008) 024903.

[41] S. Puławski, *Identification and analysis of charged hadrons in p+p interactions from NA61/SHINE experiment at CERN SPS energies*. PhD thesis, University of Silesia, Katowice, 2015. https://edms.cern.ch/file/1550661/1/main.pdf.

[42] T. Sjöstrand, S. Mrenna, and P. Skands *J. High Energy Phys.* **05** (2006) 026.

[43] P. Skands *Phys. Rev. D* **82** (2010) 074018. see arXiv:1005.3457 [hep-ph] for the newest tunes.

[44] B. B. Back *et al.*, [E917 Collab.] *Phys. Rev. C* **69** (2004) 054901.

[45] T. Anticic *et al.*, [NA49 Collab.] *Phys. Rev. Lett.* **93** (2004) 022302.

The NA61/SHINE Collaboration

A. Aduszkiewicz[15], E.V. Andronov[21], T. Antićić[3], V. Babkin[19], M. Baszczyk[13], S. Bhosale[10], A. Blondel[23], M. Bogomilov[2], A. Brandin[20], A. Bravar[23], W. Bryliński[17], J. Brzychczyk[12], M. Buryakov[19], O. Busygina[18], A. Bzdak[13], H. Cherif[6], M. Ćirković[22], M. Csanad[7], J. Cybowska[17], T. Czopowicz[17], A. Damyanova[23], N. Davis[10], M. Deliyergiyev[9], M. Deveaux[6], A. Dmitriev[19], W. Dominik[15], P. Dorosz[13], J. Dumarchez[4], R. Engel[5], G.A. Feofilov[21], L. Fields[24], Z. Fodor[7,16], A. Garibov[1], M. Gaździcki[6,9], O. Golosov[20], V. Golovatyuk[19], M. Golubeva[18], K. Grebieszkow[17], F. Guber[18], A. Haesler[23], S.N. Igolkin[21], S. Ilieva[2], A. Ivashkin[18], S.R. Johnson[25], K. Kadija[3], E. Kaptur[14], N. Kargin[20], E. Kashirin[20], M. Kiełbowicz[10], V.A. Kireyeu[19], V. Klochkov[6], V.I. Kolesnikov[19], D. Kolev[2], A. Korzenev[23], V.N. Kovalenko[21], K. Kowalik[11], S. Kowalski[14], M. Koziel[6], A. Krasnoperov[19], W. Kucewicz[13], M. Kuich[15], A. Kurepin[18], D. Larsen[12], A. László[7], T.V. Lazareva[21], M. Lewicki[16], K. Łojek[12], B. Łysakowski[14], V.V. Lyubushkin[19], M. Maćkowiak-Pawłowska[17], Z. Majka[12], B. Maksiak[11], A.I. Malakhov[19], D. Manić[22], A. Marchionni[24], A. Marcinek[10], A.D. Marino[25], K. Marton[7], H.-J. Mathes[5], T. Matulewicz[15], V. Matveev[19], G.L. Melkumov[19], A.O. Merzlaya[12], B. Messerly[26], Ł. Mik[13], S. Morozov[18,20], S. Mrówczyński[9], Y. Nagai[25], M. Naskręt[16], V. Ozvenchuk[10], V. Paolone[26], M. Pavin[4,3], O. Petukhov[18], R. Płaneta[12], P. Podlaski[15], B.A. Popov[19,4], B. Porfy[7], M. Posiadała-Zezula[15], D.S. Prokhorova[21], D. Pszczel[11], S. Puławski[14], J. Puzović[22], M. Ravonel[23], R. Renfordt[6], E. Richter-Wąs[12], D. Röhrich[8], E. Rondio[11], M. Roth[5], B.T. Rumberger[25], M. Rumyantsev[19], A. Rustamov[1,6], M. Rybczynski[9], A. Rybicki[10], A. Sadovsky[18], K. Schmidt[14], I. Selyuzhenkov[20], A.Yu. Seryakov[21], P. Seyboth[9], M. Słodkowski[17], P. Staszel[12], G. Stefanek[9], J. Stepaniak[11], M. Strikhanov[20], H. Ströbele[6], T. Šuša[3], A. Taranenko[20], A. Tefelska[17], D. Tefelski[17], V. Tereshchenko[19], A. Toia[6], R. Tsenov[2], L. Turko[16], R. Ulrich[5], M. Unger[5], F.F. Valiev[21], D. Veberič[5], V.V. Vechernin[21], A. Wickremasinghe[26], Z. Włodarczyk[9], A. Wojtaszek-Szwarc[9], O. Wyszyński[12], L. Zambelli[4], E.D. Zimmerman[25], and R. Zwaska[24]

[1] National Nuclear Research Center, Baku, Azerbaijan
[2] Faculty of Physics, University of Sofia, Sofia, Bulgaria
[3] Ruđer Bošković Institute, Zagreb, Croatia
[4] LPNHE, University of Paris VI and VII, Paris, France
[5] Karlsruhe Institute of Technology, Karlsruhe, Germany
[6] University of Frankfurt, Frankfurt, Germany
[7] Wigner Research Centre for Physics of the Hungarian Academy of Sciences, Budapest, Hungary
[8] University of Bergen, Bergen, Norway
[9] Jan Kochanowski University in Kielce, Poland
[10] Institute of Nuclear Physics, Polish Academy of Sciences, Cracow, Poland
[11] National Centre for Nuclear Research, Warsaw, Poland
[12] Jagiellonian University, Cracow, Poland
[13] AGH - University of Science and Technology, Cracow, Poland
[14] University of Silesia, Katowice, Poland
[15] University of Warsaw, Warsaw, Poland
[16] University of Wrocław, Wrocław, Poland
[17] Warsaw University of Technology, Warsaw, Poland
[18] Institute for Nuclear Research, Moscow, Russia
[19] Joint Institute for Nuclear Research, Dubna, Russia
[20] National Research Nuclear University (Moscow Engineering Physics Institute), Moscow, Russia
[21] St. Petersburg State University, St. Petersburg, Russia

[22] University of Belgrade, Belgrade, Serbia
[23] University of Geneva, Geneva, Switzerland
[24] Fermilab, Batavia, USA
[25] University of Colorado, Boulder, USA
[26] University of Pittsburgh, Pittsburgh, USA